Eastern Pacific Intraseasonal Variability: A Predictability Perspective

J. M. NEENA AND XIANAN JIANG

Joint Institute for Regional Earth System Science and Engineering, University of California, Los Angeles, Los Angeles, California

DUANE WALISER

Joint Institute for Regional Earth System Science and Engineering, University of California, Los Angeles, Los Angeles, and Jet Propulsion Laboratory, California Institute of Technology, Pasadena, California

JUNE-YI LEE

International Pacific Research Center, and Department of Meteorology, University of Hawai'i at Mānoa, Honolulu, Hawaii, and Institute of Environmental Studies, Pusan National University, Busan, South Korea

BIN WANG

International Pacific Research Center, and Department of Meteorology, University of Hawai'i at Mānoa, Honolulu, Hawaii

(Manuscript received 7 May 2014, in final form 3 September 2014)

ABSTRACT

The eastern Pacific (EPAC) warm pool is a region of strong intraseasonal variability (ISV) during boreal summer. While the EPAC ISV is known to have large-scale impacts that shape the weather and climate in the region (e.g., tropical cyclones and local monsoon), simulating the EPAC ISV is still a great challenge for present-day global weather and climate models. In the present study, the predictive skill and predictability of the EPAC ISV are explored in eight coupled model hindcasts from the Intraseasonal Variability Hindcast Experiment (ISVHE). Relative to the prediction skill for the boreal winter Madden–Julian oscillation (MJO) in the ISVHE (~15–25 days), the skill for the EPAC ISV is considerably lower in most models, with an average skill around 10 days. On the other hand, while the MJO exhibits a predictability of 35–45 days, the predictability estimate for the EPAC ISV is 20–30 days. The prediction skill was found to be higher when the hindcasts were initialized from the convective phase of the EPAC ISV as opposed to the subsidence phase. Higher prediction skill was also found to be associated with active MJO initial conditions over the western Pacific (evident in four out of eight models), signaling the importance of exploring the dynamic link between the MJO and the EPAC ISV. The results illustrate the possibility and need for improving dynamical prediction systems to facilitate more accurate and longer-lead predictions of the EPAC ISV and associated weather and short-term climate variability.

1. Introduction

The eastern Pacific warm pool is a region of strong intraseasonal variability (ISV) during boreal summer. The 30–50 days (hereafter 40 day) ISV mode of the eastern Pacific (EPAC) is largely characterized by eastward propagation of convective anomalies (Knutson and Weickmann 1987; Kayano and Kousky 1999; Maloney and Hartmann 2000a; and many others). Besides the 40-day mode, a quasi-biweekly mode of about 16-day periodicity is also prominent over the EPAC domain (Jiang and Waliser 2009; Kikuchi and Wang 2009; Wen et al. 2011). In addition to the eastward propagation, the EPAC ISV also exhibits a northward propagating component, possibly due to the presence of strong vertical zonal wind shear over the EPAC warm pool (Jiang and Waliser 2008; Maloney et al. 2008). Even though the

Corresponding author address: J. M. Neena, Jet Propulsion Laboratory, 4800 Oak Grove Dr., MS 233-300, Pasadena, CA 91109.
E-mail: neena.j.mani@jpl.nasa.gov

DOI: 10.1175/JCLI-D-14-00336.1

EPAC ISV is restricted to a relatively small tropical domain, it exerts widespread influences on the regional weather and climate. It impacts and modulates the tropical cyclone activity over the EPAC and the Gulf of Mexico (e.g., Maloney and Hartmann 2000a,b; Jiang et al. 2012), the summertime wind jets and precipitation (Serra et al. 2010; Martin and Schumacher 2011; Moon et al. 2013), the North American monsoon (Higgins and Shi 2001; Lorenz and Hartmann 2006), and midsummer droughts over Central America and Mexico (Magaña et al. 1999; Small et al. 2007).

Notwithstanding the regional impacts of the EPAC ISV, efforts toward understanding and simulating the EPAC ISV are rather limited (e.g., Maloney and Kiehl 2002; Maloney and Esbensen 2005; Maloney et al. 2014) when compared to the numerous studies focused on the Madden–Julian oscillation (MJO) (Lau and Waliser 2012; Zhang 2005, and references therein). J. Lin et al. (2008), in one of the earliest assessment of the general circulation models (GCMs) ability in simulating the EPAC ISV, based on model simulations from phase 3 of the Coupled Model Intercomparison Project (CMIP3), showed that generally most GCMs underestimated the intraseasonal precipitation variance over the EPAC warm pool and often failed to capture the eastward propagation of convective anomalies. In a recent study by Jiang et al. (2013), it was shown that out of 16 GCMs included in phase 5 of CMIP (CMIP5), only seven GCMs were able to capture the spatial pattern of the leading EPAC ISV mode in precipitation; and even in these GCMs the biases in simulating EPAC ISV amplitude were quite large. On the other hand, another multimodel evaluation by Jiang et al. (2012) noted that higher-resolution models with improved representation of deep convection were more skillful in simulating the EPAC ISV modes. While these studies evaluated GCM capabilities in simulating the intrinsic EPAC ISV mode, assessing the prediction capabilities in GCMs for the EPAC ISV mode is an area that has never been explored. The past decade has witnessed significant improvement in dynamical prediction skill for the MJO (e.g., Seo et al. 2009; Vitart and Molteni 2010; Rashid et al. 2011; Waliser 2011; Zhang and Van den Dool 2012; Wang et al. 2014; Neena et al. 2014). Assessing the EPAC ISV prediction skill in a suite of contemporary GCMs would be of considerable value for the ISV forecasting efforts, for the North and Central American regions in particular.

Understanding the inherent predictability of the EPAC ISV mode is another aspect essential for framing prediction efforts and assessing their skill. While many earlier studies have explored the predictability (perfect model) for other ISV modes (Waliser et al. 2003a,b; Liess et al. 2005; Fu et al. 2007; Pegion and Kirtman 2008; Neena and Goswami 2010), the predictability of the EPAC ISV mode has never been estimated. In the present study, based on hindcasts from eight different coupled GCMs participating in the Intraseasonal Variability Hindcast Experiment (ISVHE), estimates of prediction skill and predictability of the EPAC ISV are reported for the first time. The prediction skill and predictability of the winter MJO and Asian summer monsoon ISV in these models have been explored in two companion studies (Neena et al. 2014; J. Lee et al. 2014, unpublished manuscript).

Another aspect of interest concerning the EPAC ISV is its association with the MJO and/or boreal summer intraseasonal oscillation (BSISO). The EPAC warm pool represents a region with the largest MJO influences on regional precipitation variability, outside the Indo-Pacific warm pool. Because of its dominant eastward propagating character, the EPAC ISV was often considered a local expression of the global MJO mode (Knutson and Weickmann 1987; Kayano and Kousky 1999; Maloney and Hartmann 2000a; and many others), initiated by eastward propagation of convective signals across the date line from the western Pacific (Maloney and Esbensen 2007; Maloney et al. 2008). Moon et al. (2013) further showed that the EPAC ISV is closely linked with the ISV over the Indian and western North Pacific summer monsoon region. However, modeling studies showed that in several GCMs, which exhibited realistic simulations of the EPAC ISV, the physical link between western Pacific MJO convection and the EPAC ISV was not always evident. In these GCM simulations, the EPAC ISV convective signals often originate from the central Pacific between 150°E and 150°W (Jiang et al. 2012, 2013). This finding indicated that the EPAC ISV could be a local mode with an existence independent of the eastward propagating MJO.

The observed phase locking of EPAC ISV convective activity with that over the Indo-Pacific warm pool (e.g., Wang et al. 2006; Maloney and Esbensen 2007; Maloney et al. 2008; Jiang et al. 2012; Moon et al. 2013) suggests that one or more remote forcing mechanisms might be at work, linking the intraseasonal convective activity over the two regions. Wang et al. (2006) associated the see-saw pattern of convective activity between the EPAC and the eastern Indian Ocean domain with stationary pulses of the Walker circulation and suggested a mechanism of communication involving upper-level divergent waves. Based on a regional coupled model experiment, Small et al. (2011) proposed that fast propagating dry Kelvin waves, generated in response to the intraseasonal convective activity over the western Pacific, could be responsible for the reinitiation of

opposite phase of convection over the eastern Pacific. The relative roles of local convection–circulation feedbacks and the proposed mechanism of MJO remote forcing in maintaining the EPAC ISV were investigated in a modified version of the National Center for Atmospheric Research (NCAR) Community Atmosphere Model (CAM), version 3.1, and the International Pacific Research Center (IPRC) Regional Atmosphere Model (IRAM) by Rydbeck et al. (2013). They found that while the EPAC ISV could be initiated and sustained in the CAM even in the absence of remote forcing from the western Pacific, the regionally generated EPAC ISV was found to be weak and incoherent when cut off from all remote intraseasonal signals. However, a clear insight into the EPAC ISV–MJO relationship was not afforded from the study mainly because of the model discrepancies in simulating the EPAC ISV. A well-designed experimental framework based on a suite of models with reasonably good EPAC ISV simulation capability, might provide some interesting insight to this problem. While such an analysis is not the focus and beyond the scope of the present study, we will try to further characterize the MJO–EPAC ISV relationship using observed data, particularly in the context of its possible impacts on EPAC ISV prediction skill.

The manuscript is structured as follows. In section 2, details of the ISVHE hindcast data are provided and a brief description of the method to estimate prediction skill and predictability is provided. Isolation of the leading EPAC ISV modes based on the observations is dealt with in section 3. In section 4, the prediction skill estimation for the EPAC ISV in the eight model hindcasts is reported. Details of the predictability estimation approach and the predictability estimates for the EPAC ISV in the eight models are presented in section 5. The EPAC ISV–MJO relationship is explored in section 6 and the influences of MJO remote forcing on the EPAC ISV hindcast skill in different models are estimated. The summary and conclusions from the study are provided in section 7.

2. Data and approaches

We analyze the hindcasts for the boreal summer season (May–September) from eight coupled models that participated in the ISVHE project, including two versions of the Australian Bureau of Meteorology (BoM) coupled model (ABOM1 and ABOM2), two versions of the National Centers for Environmental Prediction (NCEP)/Climate Prediction Center (CPC) coupled models [Climate Forecast System (CFS) versions 1 and 2 (CFS1 and CFS2)], the European Centre for Medium-Range Weather Forecasts (ECMWF) model, the Japan Meteorological Agency (JMA) coupled model (JMAC), the coupled model of the Centro Euro-Mediterraneo per i Cambiamenti Climatici (CMCC), and the Seoul National University (SNU) coupled model (SNUC). For further details of the ISVHE project and the participating models, please refer to J. Lee et al. (2014, unpublished manuscript) and Neena et al. (2014). While we have used all the available years of data [Table 1 of Neena et al. (2014)] in the predictability estimation, the prediction skill estimates are based on data starting 1998 [for verification against the Tropical Rainfall Measuring Mission (TRMM) 3B42 precipitation–based estimates]. Daily fields of the TRMM 3B42 precipitation (Huffman et al. 2007) and 850-hPa zonal wind (U850) fields from the ECMWF Interim Re-Analysis (ERA-Interim; Dee et al. 2011) are used for deriving the EPAC ISV mode and as the verifying analyses in the prediction skill estimation. The Real-Time Multivariate MJO (RMM) indices (Wheeler and Hendon 2004, hereafter WH04) from 1979 to 2012 were obtained from http://cawcr.gov.au/staff/mwheeler/maproom/RMM/. The newly developed all-season outgoing longwave radiation (OLR)-based MJO index (OMI; Kiladis et al. 2014) for the period was obtained from http://www.esrl.noaa.gov/psd/mjo/mjoindex/. The OMI represents the principal components (PCs) obtained by projecting 20–96-day time filtered OLR onto the two dominant daily empirical orthogonal function (EOF) modes of 30–96-day eastward filtered OLR See Kiladis et al. (2014) for further details of the OMI.

The commonly used correlation-based approach (e.g., H. Lin et al. 2008; Rashid et al. 2011) is adopted for the prediction skill estimation of the EPAC ISV based on the model hindcasts. Skill is also estimated following the signal-to-noise ratio approach as in Neena et al. (2014). This signal-to-noise ratio approach was also employed to estimate the predictability of the leading ISV mode. Two estimates of predictability are attempted, namely a single-member predictability estimate and an ensemble-mean predictability estimate. For the single-member predictability estimate, a single member hindcast is evaluated against every other member hindcast in a perfect model sense. In the ensemble-mean predictability estimate, a given ensemble member hindcast is evaluated against the ensemble-mean hindcast involving all the other ensemble members. These approaches have been used for estimating the winter MJO predictability in the same eight model hindcasts by Neena et al. (2014). More details of the estimation are provided in section 6 as well as in Neena et al. (2014). While the estimates of average and ensemble-mean prediction skill would give an assessment of the actual prediction capability for the EPAC ISV in dynamical models, the perfect model predictability estimates using single-member and ensemble-mean

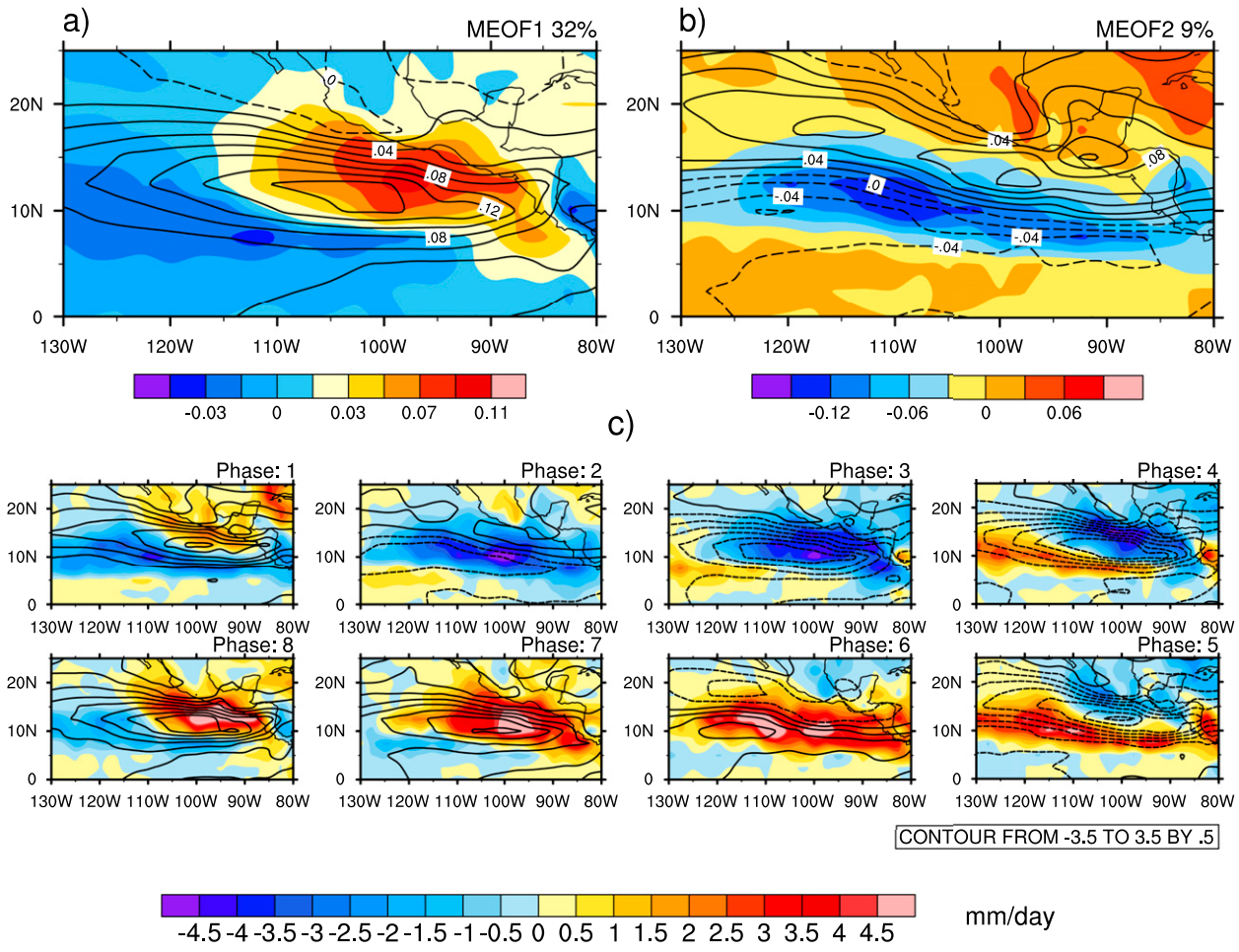

FIG. 1. (a),(b) The first two MEOF patterns ($MEOF1_{obs}$ and $MEOF2_{obs}$) of 20–100-day filtered daily anomalies of TRMM 3B42 precipitation (shaded, mm day^{-1}) and ERA-Interim U850 (contours, m s^{-1}) for the May–September (MJJAS) season from 1998 to 2012, over the eastern Pacific domain (0°–25°N, 130°–80°W). The percentage of variance explained by the MEOF patterns is given at the top right-hand corners of the panels. (c) Composites of 20–100-day filtered TRMM 3B42 precipitation (shaded) and ERA-Interim U850 (contours) anomalies for the eight phases of EPAC ISV evolution (clockwise, beginning from top left) defined by the principal components of the two MEOF patterns. The contours range from −3.5 to 3.5 m s^{-1} with an interval of 0.5. Solid (dashed) contours represent positive (negative) values.

approaches would help us gauge the unexplored potential for predicting the EPAC ISV mode.

3. The EPAC ISV mode

The leading EPAC ISV mode is isolated by conducting an EOF analysis of the combined fields of 20–100-day filtered daily TRMM precipitation and ERA-Interim U850 anomalies over the EPAC domain of 0°–25°N, 130°–80°W for the May–September season from 1998 to 2012. Before computing the EOF of the combined fields, the filtered precipitation and U850 fields are first normalized by the corresponding temporal standard deviation values. It has been shown by many previous studies that multivariate EOF (MEOF) analysis is a very useful approach for extracting dominant intraseasonal signals (e.g., Wang 1992; WH04; Lee et al. 2013). The first two MEOF modes ($MEOF1_{obs}$ and $MEOF2_{obs}$) explains 32% and 9% of the variance (Figs. 1a and 1b) respectively, and represent the propagating facets of the EPAC ISV. While $MEOF1_{obs}$ captures the north–south dipole mode of convection over the EPAC domain, $MEOF2_{obs}$ represents an eastward shifted zonally elongated band of convection around 10°N. Maximum correlation between the two PCs is observed when $PC1_{orig}$ leads $PC2_{orig}$ by 8–10 days (correlation of 0.53; not shown). Based on the first two PCs, eight phases of the EPAC ISV were then defined analogously to the MJO RMM indices (WH04). Composites of 20–100-day filtered precipitation and U850 anomalies for the eight

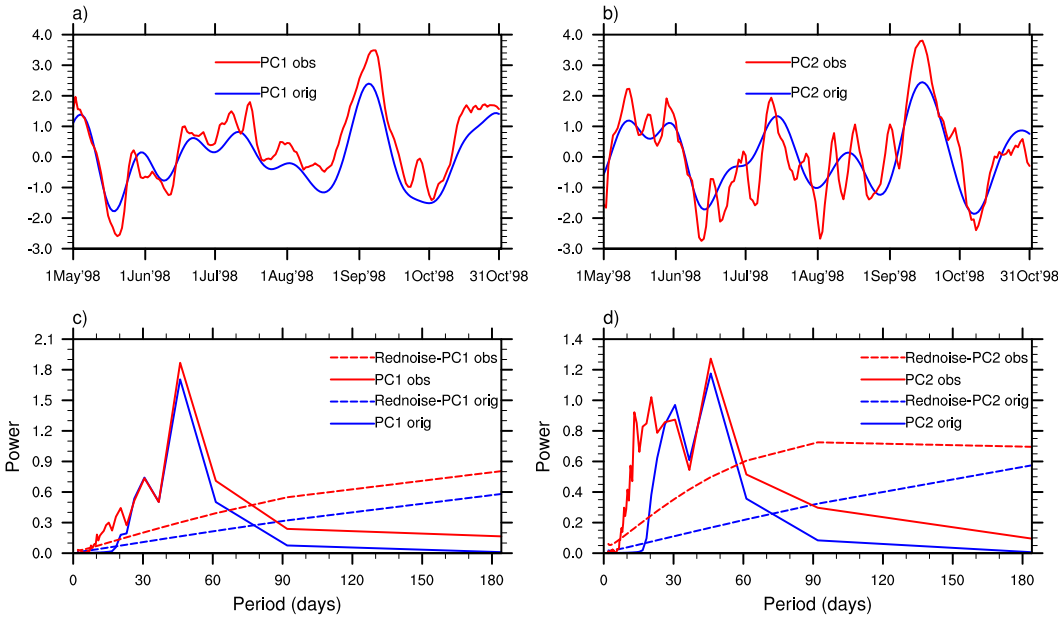

FIG. 2. (a),(b) The principal component time series obtained by projecting 20–100-day filtered anomalies ($PC1_{orig}$ and $PC2_{orig}$, blue lines) and 5-day running mean smoothed anomalies ($PC1_{obs}$ and $PC2_{obs}$, red lines) onto the two dominant MEOF modes, for the May–October 1998 season. (c),(d) The average power spectra (over 15 yr, 1998–2012) and the corresponding red noise spectra for $PC1_{orig}$ and $PC2_{orig}$ (blue) shown along with those for $PC1_{obs}$ and $PC2_{obs}$ (red).

ISV phases are shown in Fig. 1c. The northeastward propagation of the EPAC ISV convective anomalies (cf. Jiang and Waliser 2008) are clearly evident from the phase composites. Phases 2–4 capture the evolution of negative precipitation anomalies over the EPAC, while phases 6–8 represent the convective phase of the EPAC ISV.

The PC time series ($PC1_{orig}$ and $PC2_{orig}$) for the May–October 1998 season are shown in Figs. 2a and 2b (blue lines). The average power spectra (over 15 yr) of $PC1_{orig}$ and $PC2_{orig}$ suggest a prevailing period of about 40–50 days associated with the leading ISV mode (Figs. 2c,d, blue curves). In addition to the 40–50-day spectral peak, a secondary peak around 30 days is also evident in $PC2_{orig}$, which could be associated with the quasi-biweekly ISV mode reported over the EPAC, to be further discussed below (e.g., Jiang and Waliser 2009). The purpose of the study is to estimate the prediction skill and predictability of the EPAC ISV, and in the following sections we derive the PCs from model hindcasts. Since the model hindcasts are of short length, applying a 20–100-day bandpass filter is not viable and to filter out the weather-scale variability (at least partly) without losing many data points, we apply a 5-day running mean filter to the hindcast data. To test the feasibility of the PCs obtained in this manner, the observed PCs were also derived by projecting the 5-day running mean smoothed anomalies onto the $MEOF_{obs}$, and the resultant PCs are referred to as $PC1_{obs}$ and $PC2_{obs}$. The red lines in Figs. 2a and 2b represent the $PC1_{obs}$ and $PC2_{obs}$ from May to October 1998. The average power spectra for $PC1_{obs}$ and $PC2_{obs}$ during 15 summers are shown as the red curves in Figs. 2c and 2d. It is seen that $PC1_{obs}$ is quite similar to $PC1_{orig}$ (correlation of 0.92), with both exhibiting a 40-day spectral peak. In contrast, $PC2_{obs}$ retains considerably more high-frequency variability than $PC2_{orig}$ (correlation of 0.82). The presence of the quasi-biweekly EPAC ISV mode is clearly evident in the $PC2_{obs}$ power spectra, with a secondary spectral peak in the 10–30-day period range. The aforementioned spectral peak at about 30 days in the $PC2_{orig}$ spectra (blue curve in Fig. 2c) seems to be the result of the cutoff at 20 days resulting from bandpass time filtering. Hence, cautions need to be exercised that while $MEOF1_{obs}$ and $MEOF2_{obs}$ together represent the leading 40-day ISV mode over the EPAC, the spatial pattern of the $MEOF2_{obs}$ in particular may also represent part of signals of the high-frequency ISV mode over the EPAC. This needs to be borne in mind when evaluating the predictive skill of EPAC ISV in model hindcasts as to be dealt with in section 4.

4. Prediction skill for the EPAC ISV

The hindcast skill for the EPAC ISV in the eight models is estimated using the PCs ($PC1_{hcast}$ and $PC2_{hcast}$ hereafter)

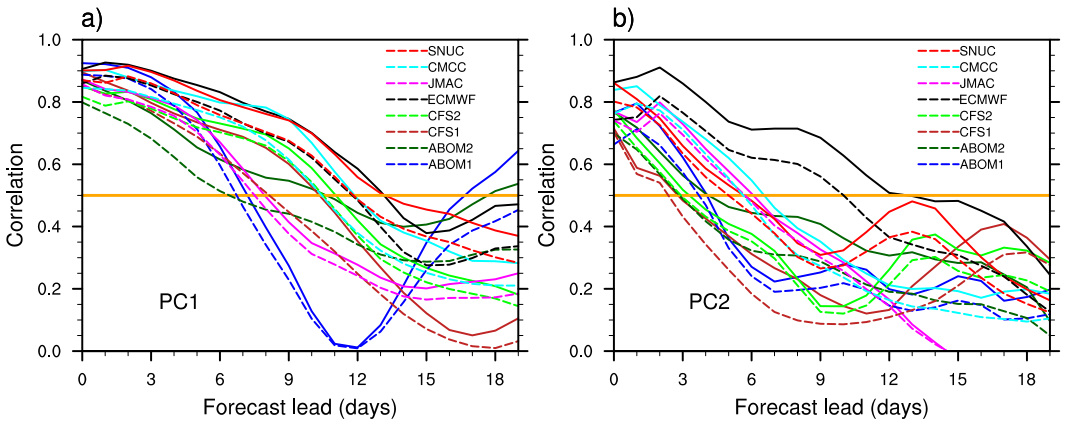

FIG. 3. (a) Correlation between $PC1_{obs}$ and $PC1_{hcast}$ values (y axis) in the eight coupled models as a function of forecast lead (x axis; days). Correlations corresponding to individual hindcasts (ensemble-mean hindcasts) are shown as dashed (solid) lines. The corresponding prediction skill estimates are marked by the forecast lead at which the correlation drops below a 0.5 threshold (orange solid line). (b) As in (a), but for observed and hindcast PC2.

derived by projecting daily hindcast anomalies of precipitation and U850 onto $MEOF1_{obs}$ and $MEOF2_{obs}$. This method of forecast skill estimation has been employed by many earlier studies (e.g., Vitart et al. 2007; H. Lin et al. 2008; Seo et al. 2009). The preprocessing steps involve the computation of daily hindcast anomalies by removing the hindcast climatology from the daily fields and applying a 5-day running mean to the anomalies to remove some of the high-frequency synoptic scale variability. Note that while a 20–100-day bandpass time filtering was applied to derive the two leading MEOF modes of the EPAC ISV from the observations, both the hindcast PCs and the observed PCs used for verification are computed using 5-day running mean smoothed anomalous fields. Without bandpass filtering the PC time series corresponding to $MEOF2_{obs}$ may retain significant signals associated with the quasi-biweekly ISV mode and other high-frequency modes (see Fig. 2b). Hence we have refrained from estimating the combined prediction skill and predictability for the two leading PCs but rather have made estimates separately for PC1 and PC2.

The hindcast skill for the EPAC ISV in the models is measured as the hindcast lead day at which the correlation between $PC1_{hcast}$ ($PC2_{hcast}$) and $PC1_{obs}$ ($PC2_{obs}$) falls below a 0.5 threshold. Figures 3a and 3b illustrate the average individual hindcast prediction skill (dashed lines) and the ensemble-mean prediction skill (solid lines) in the eight models for PC1 and PC2, respectively. The prediction skill estimates are based on hindcasts for which the EPAC ISV amplitude, defined by $(PC1^2_{orig} + PC2^2_{orig})^{1/2}$, was greater than 1.0 on the day of hindcast initiation. The ECMWF, CFS2, CMCC, and SNU models exhibit maximum prediction skill for PC1 in individual hindcasts, with an average skill of 10–12 days. It is noteworthy that the average prediction skill for the boreal winter MJO based on the same eight models is about 15 days, with the ECMWF model showing the highest skill of 19 days (Neena et al. 2014). Also note that the largest skill improvement for the EPAC ISV achieved by ensemble-mean hindcasts over the individual hindcasts is about 2–4 days, which is considerably lower than the 8–10-day skill improvement found for the boreal winter MJO (Neena et al. 2014; J. Lee et al. 2014, unpublished manuscript). While the PC2 hindcast skill is 10 days in the ECMWF model, it is less than 7 days in all other models. As discussed in the previous section, the $PC2_{hcast}$ and $PC2_{obs}$ may be contaminated by high-frequency ISV variability; therefore, the PC2 skill in most models may not purely reflect the skill for the leading 40-day ISV mode over the EPAC.

Next, prediction skill for the EPAC ISV is explored separately for the convective and subsidence phases of the EPAC ISV. For any model, the hindcasts were divided into two groups: the convective phase (phases 6–8) and the subsidence phase (phases 2–4), based on the EPAC ISV phases (identified using $PC1_{orig}$ and $PC2_{orig}$) and the EPAC ISV amplitude being greater than 1.0 on the day of hindcast initiation. Hindcasts were initialized during the ISV transition phases; phases 1 and 5 were not included. Examination of the average prediction skill for PC1 for these two cases (Fig. 4) shows that in most of the models, hindcasts initialized from the EPAC ISV convective phases (red bars) exhibits higher average prediction skill than those initialized from subsidence phases (blue bars). The 95% confidence estimates for the correlation based skill score are represented by the error bars in Fig. 4. For estimating the 95% confidence estimates, a Fisher Z' transformation is applied to the correlation coefficient (Fisher 1921;

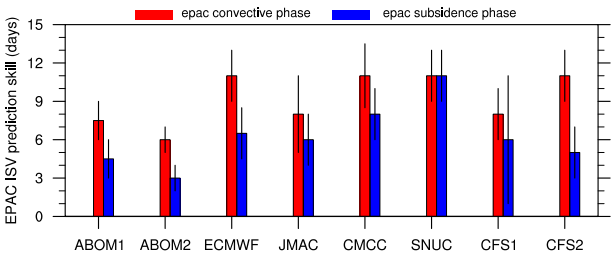

FIG. 4. Average individual hindcast prediction skill for PC1 for hindcasts initiated from EPAC ISV convective phase (phases 6–8; red bars) and EPAC ISV subsidence phase (phases 2–4; blue bars). The error bars represent the 95% confidence estimates for the correlation based prediction skill.

the correlation coefficient is transformed to a variable that is normally distributed with a known standard error) at each hindcast lead day. The confidence interval is estimated corresponding to a standard normal distribution and an inverse transform is used to obtain the corresponding correlation limits. The lead day of hindcast for which the confidence limits of the correlation coefficient falls below the 0.5 threshold is used to define the confidence limits of prediction skill shown in Fig. 4. In ABOM1, ABOM2, ECMWF, and CFS2, the difference between the correlation-based skill scores for convective and subsidence phases (red and blue bars) are larger than the combined error for the two skill score estimates at 95% confidence (the error bars do not overlap). Hence the difference in skill for these models can be considered to be statistically significant.

5. Predictability of the EPAC ISV

The predictability of the EPAC ISV mode is measured using the same two approaches as in Neena et al. (2014), namely, single-member predictability estimate and ensemble-mean predictability estimate. For the single-member predictability estimate, a single member of the ensemble is considered as the control hindcast, and every other ensemble member is regarded as a perturbed hindcast. For the ensemble-mean predictability estimate, any given member hindcast is considered as the control hindcast, and the ensemble mean from all other members is considered as the perturbed hindcast. The $PC1_{hcast}$ and $PC2_{hcast}$ estimates from the control and perturbed hindcasts are analyzed. The "error" or divergence of the PC trajectories is measured as the squared difference between control and perturbed hindcast $PC1_{hcast}$ and $PC2_{hcast}$ values, as a function of lead time. The "signal" is defined as the average variance of the control hindcast PC over a 41-day sliding window. A 41-day window was chosen as it covers a full cycle of the EPAC ISV. The results were found to be consistent for a 46- or 51-day choice of window length. Predictability for the corresponding PC is then defined as the hindcast lead at which the error becomes as large as the signal (e.g., Waliser et al. 2003a,b; Pegion and Kirtman 2008). The details of the single-member and ensemble-mean predictability estimation methods can be found in Neena et al. (2014). The only variation in the approach in this study is that we make individual predictability estimates for $PC1_{hcast}$ and $PC2_{hcast}$, rather than a combined estimate as in Neena et al. (2014). As shown in the following Eq. (1), the mean square error for each lead day j is computed over a total $N \times m_1$ cases (m_1 is the number of possible control-perturbed pairs for a given initial condition and N gives the total number of initial conditions). For the ensemble-mean estimate, m_1 is equal to the ensemble size nk. For the single-member predictability estimate m_1 takes the value of nk − 1 factorial when all the ensemble members are initialized the same day, while it counts only those ensemble pairs initialized with a maximum separation of 1 day when the ensemble members are initialized from time-lagged initial conditions:

$$\langle E_j^2 \rangle \equiv \frac{1}{N \times m_1} \sum_{i=1}^{N} \sum_{m_1 \text{ control perturbed pairs}} (\mathrm{PC}_{ij}^{\text{control}} - \mathrm{PC}_{ij}^{\text{perturbed}})^2 . \quad (1)$$

The mean signal [Eq. (2)] is computed over a total $N \times$ nk control cases as a function of lead day j, as follows. The observed PC values ($PC1_{obs}$ and $PC2_{obs}$) prior to hindcast initiation day were also used in the sliding window variance computation:

$$\langle S_j^2 \rangle \equiv \frac{1}{N \times \text{nk}} \sum_{i=1}^{N} \sum_{\text{nk control}} \left[\frac{1}{41} \sum_{t=-20}^{20} (\mathrm{PC}_{ij}^{\text{control}})^2 \right] . \quad (2)$$

The single-member and ensemble-mean estimates of predictability for the two PCs are shown in Fig. 5. Figures 5a and 5b show the mean square error (solid blue: single-member method; solid black: ensemble-mean method) and mean signal (solid red) estimates based on each model hindcast for $PC1_{hcast}$ and $PC2_{hcast}$, respectively. The 95% confidence estimates (obtained based on a Student's t test) for both error and signal are shown as dashed lines. For PC1, the single-member

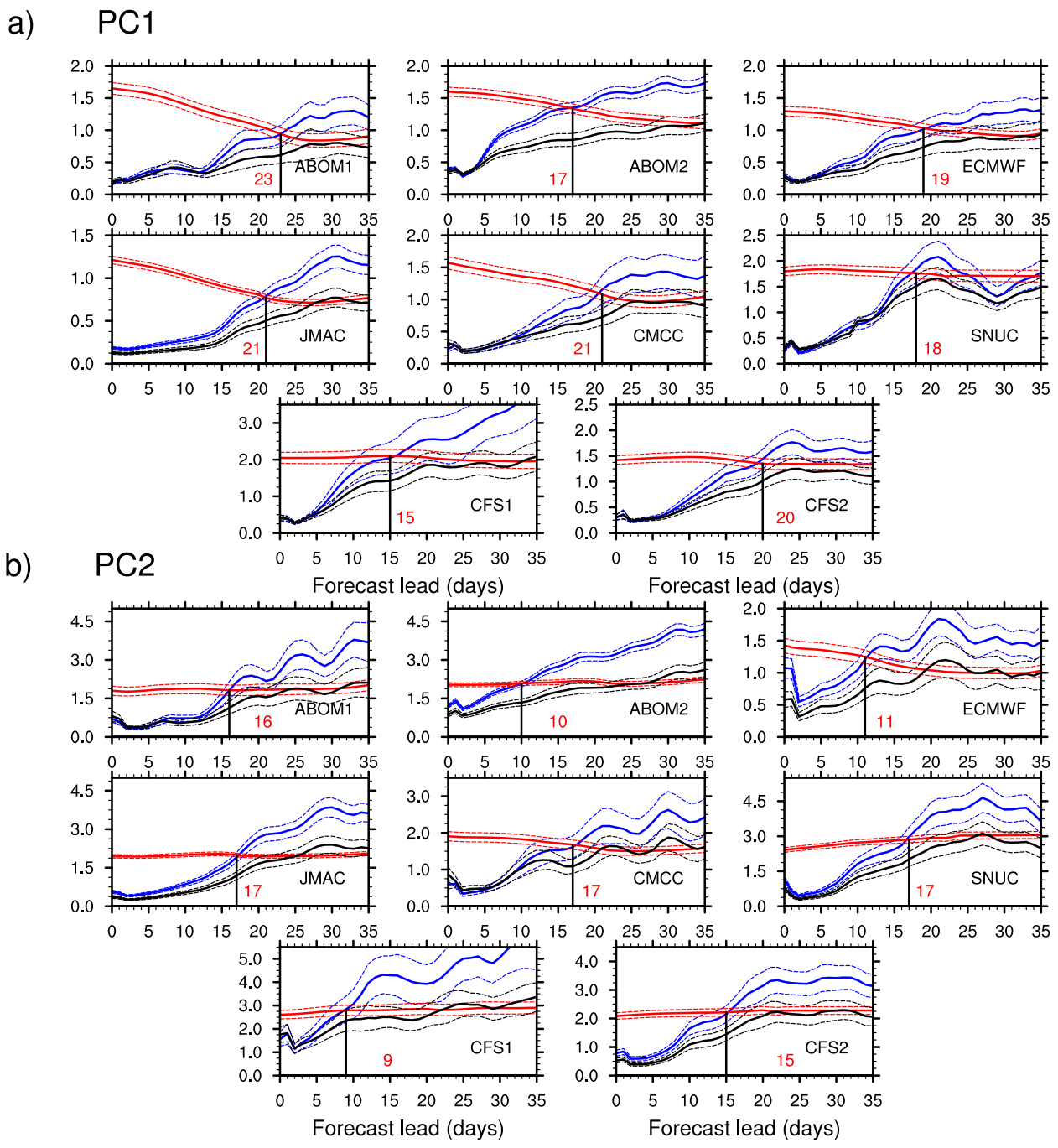

FIG. 5. (a) Average error and signal estimates for PC1 in the eight models. Saturation of the blue solid error growth curve (single-member estimate) with respect to the signal (red solid) marks the predictability for individual hindcasts (denoted by the black vertical line along with the corresponding number of forecast lead day in red in each panel) and saturation of the black solid error growth curve (ensemble-mean estimate) with respect to the signal (red solid) marks the predictability for ensemble-mean hindcasts. Shown as dashed lines are the 95% confidence estimates for error and signal. (b) As in (a), but for PC2. Note the *y*-axis scale is not uniform in the panels of (a) and (b).

predictability estimates from the eight models ranges from 15 to 23 days with an average value of 19 days, whereas that based on the ensemble-mean approach extends to a 20–30-day range. The predictability for PC2 is much lower, ranging from 9 to 17 days for single-member estimate and about 21 days for ensemble-mean estimate. Although an average predictability of 15–23 days for the EPAC ISV mode is lower than the 21–28-day

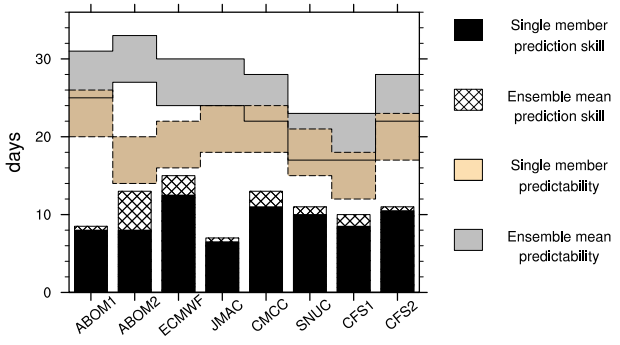

FIG. 6. Signal-to-noise ratio based estimates of prediction skill and predictability for EPAC ISV PC1 in the eight models (x axis). Average individual hindcast prediction skill estimates are shown as black bars and ensemble-mean prediction skill estimates are shown as hatched bars. A ±3-day range for single-member and ensemble-mean estimates of predictability are represented by the tan and gray shaded areas respectively.

predictability found for the boreal winter MJO in the same set of models (Neena et al. 2014), it has a similar range as the summer monsoon ISV reported by earlier studies (Liess et al. 2005; Neena and Goswami 2010). To compare against the predictability estimates based on the signal-to-noise ratio framework, the prediction skill for PC1 was estimated using the signal-to-noise ratio approach. For estimating prediction skill, $PC1_{obs}$ is treated as the "control" in Eqs. (1) and (2). The average prediction skill for individual hindcasts and ensemble-mean prediction skill for PC1 in the eight models and the respective ±3-day predictability estimate ranges are shown in Fig. 6. With an average prediction skill around 10 days and limited improvement in ensemble-mean prediction skill, a 20–30-day predictability leaves a lot of room for improving the dynamic prediction of the EPAC ISV mode.

6. EPAC ISV–MJO relationship

As previously mentioned, the association between the ISV over the EPAC warm pool and the global MJO has been reported by many earlier studies. While some studies identified the EPAC ISV as regional manifestation of the global MJO (Maloney and Esbensen 2007; Maloney et al. 2008; and many others), latest modeling studies (Jiang et al. 2012, 2013; Rydbeck et al. 2013) indicated that the EPAC ISV could be sustained even in the absence of propagating MJO signals from the western Pacific. The relative roles of local convection–circulation feedbacks versus remote forcing mechanisms in initiating and maintaining the EPAC ISV are still not quite well understood. While a detailed analysis of these aspects is beyond the scope of the present study, in this section we undertake an analysis of the EPAC ISV–MJO relationship based on observation-based MEOFs and PCs and attempt to explore its possible implications on the EPAC ISV prediction skill in the ISVHE hindcasts. All the analyses are based on the summer season (May–October).

Days of strong EPAC ISV activity are identified based on the $PC1_{orig}$ and $PC2_{orig}$ time series, as when the combined amplitude of the two PCs $[(PC1^2_{orig} + PC2^2_{orig})^{1/2}]$ is greater than 1.0. Of the total number of days, 44% are found to be EPAC ISV active days. Similarly, strong MJO events are identified based on the RMM (WH04) and OMI (Kiladis et al. 2014) amplitudes. The OMI is used as an alternate MJO index since the RMM amplitude is often suspected to be influenced by projections from east Pacific wind anomalies. It is noted that 68% (55%) of EPAC ISV active days occurred in conjunction with active MJO conditions [RMM amplitude >1.0 (1.2)] and 32% (22%) of EPAC ISV active days occurred while the MJO was weak or quiescent [RMM amplitude <1.0 (0.8)]. Based on the OMI, 65% (51%) of EPAC ISV active days are found to be associated with active MJO conditions [OMI amplitude >1.0 (1.2)] and 35% (23%) of the EPAC ISV active days are associated with weak or quiescent MJO [OMI amplitude <1.0 (0.8)] (not shown).

Based on the EPAC ISV active days occurring in conjunction with active MJO conditions, we next explore whether the EPAC ISV activity bears any relationship with the phase of MJO. The EPAC ISV active days co-occurring with active MJO conditions (RMM amplitude >1.2) are divided into two sets, one representing the EPAC ISV subsidence phases (phases 2–4) and the other representing EPAC ISV convective phases (phases 6–8). For the two cases, the probability of occurrence of MJO in the eight RMM phases is explored at different lag/lead days (Figs. 7a,b). From Fig. 7a, it is evident that 82% of the EPAC ISV subsidence phase days, occurred along with active MJO convection over the western Pacific (where 82% includes RMM phases 4, 5, and 6 combined). And 88% of the EPAC ISV convective phase days are associated with MJO convection over Africa and Indian Ocean (where 88% includes RMM phases 8, 1, and 2 combined) with subsidence conditions prevailing over the western Pacific (Fig. 7b). This is in agreement with the phase locking of opposite phases of convection over the eastern and western Pacific, reported in many earlier studies (e.g., Maloney and Hartmann 2000a; Wang et al. 2006; Maloney et al. 2008). Similar results are obtained when the MJO phases are defined based on OMI (Figs. 7c,d). To facilitate direct comparison with the RMM indices, we have followed the necessary reordering of OMI PCs recommended by Kiladis et al. (2014). We found 75% of EPAC ISV

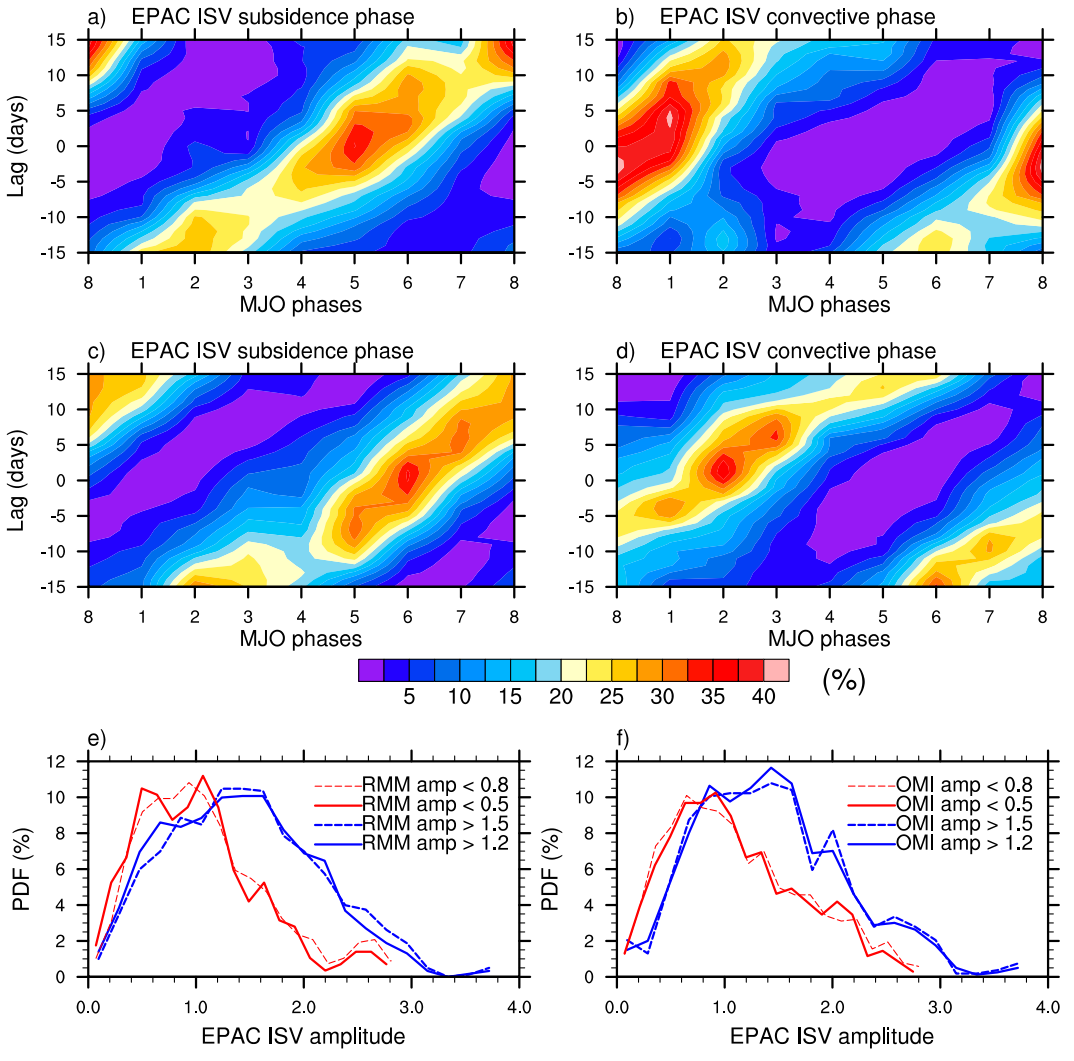

FIG. 7. (a) Probability of occurrence (shown as percentage) of MJO (RMM amplitude >1.2) in the eight RMM phases (x axis) at different lead–lag days with respect to days when the EPAC ISV (amplitude >1.0) is in its subsidence phase (EPAC ISV phases 2–4) and (b) convective phase (phases 6–8). (c),(d) As in (a),(b), but the MJO is defined by OMI. (e) The pdf of EPAC ISV amplitude associated with active MJO conditions (in blue; solid line: RMM amplitude >1.2 and dashed line: RMM amplitude >1.5) and quiescent MJO conditions (in red; solid line: RMM amplitude <0.5 and dashed line: RMM amplitude <0.8). (f) As in (e), using OMI in place of RMM.

subsidence phase days to be associated with active MJO convection over the western Pacific (where 75% includes OMI phases 5–7 combined) (Fig. 7c). Also, 85% of EPAC ISV convective phase days are associated with subsidence conditions over western Pacific (where 85% includes OMI phases 8, 1, 2, and 3 combined) (Fig. 7d). The slight eastward shift in the distributions in Figs. 7c and 7d compared to Figs. 7a and 7b might be due to slight disparities in the location and strength of convection for the MJO phases defined by the two indices. Differences in the lead–lag relationship between $PC1_{orig}$ time series with the RMM/OMI PCs could also be a contributing factor. Maximum negative correlation is observed when RMM1 leads $PC1_{orig}$ by 1–2 days, while OMI-1 exhibits maximum negative correlation when it leads $PC1_{orig}$ by 5 days. RMM2 exhibits maximum negative correlation when it lags $PC1_{orig}$ by 7–8 days. OMI-2, on the other hand, shows maximum negative correlation when it lags $PC1_{orig}$ by 5 days (not shown).

As previously mentioned, 22%–32% of active EPAC ISV days occurred in conjunction with quiescent MJO conditions. Next we explore whether the presence or absence of MJO forcing have any influences on the amplitude of EPAC ISV. To ensure better accuracy of results, well-separated thresholds are used for identifying active and quiescent MJO conditions. Figure 7e

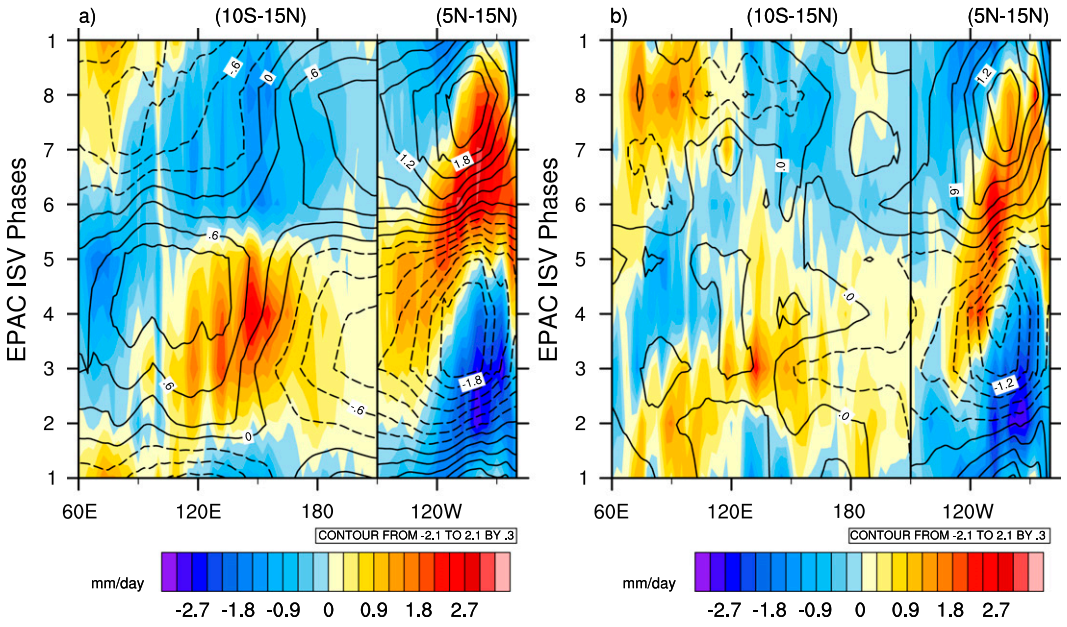

FIG. 8. The eastward propagation of 20–100-day filtered precipitation (shading, mm day^{-1}) and U850 (contours, m s^{-1}) anomalies in the composites based on the eight EPAC ISV phases concurrent with (a) active MJO conditions (RMM amplitude >1.2) and (b) quiescent MJO conditions (RMM amplitude <0.5). The time axis (y axis) is represented by the eight EPAC ISV phases. For the 60°E–150°W longitudes, the anomalies are averaged between 10°S and 15°N and for the eastern Pacific domain from 150° to 80°W, the anomalies are averaged between 5° and 15°N. The precipitation anomalies are shown in shading and the U850 anomalies are shown as contours. The contours range from −2.1 to 2.1 m s^{-1} with an interval of 0.3 m s^{-1}. Solid (dashed) contours represent positive (negative) values.

shows the probability distribution function (pdf) of EPAC ISV amplitude associated with active MJO conditions (two thresholds are considered, RMM amplitude >1.2 and >1.5) and quiescent MJO conditions (two thresholds are considered, RMM amplitude <0.8 and <0.5). It is observed that the EPAC ISV amplitude tends to be slightly skewed toward the lower-amplitude range when the MJO forcing is weak. The pdfs based on the OMI thresholds are shown in Fig. 7e and the results are very similar. Since consistent results are obtained irrespective of the index used for defining MJO, for the remaining analyses only the results based on RMM are reported.

The intraseasonal variance of precipitation over the EPAC associated with weak MJO events is found to be lower than that associated with active MJO events (not shown). This difference is further explored in the composites of 20–100-day filtered precipitation and U850 anomalies for the eight phases of the EPAC ISV, based on whether it occurred in conjunction with active (RMM amplitude >1.2) or quiescent (RMM amplitude <0.5) MJO conditions. The eastward propagation of the ISV over the eastern Pacific as well as that over the Indian Ocean/western Pacific is shown in the time–longitude profiles based on the composites during active (Fig. 8a) and quiescent (Fig. 8b) MJO conditions. The eight EPAC ISV phases are used to represent the time axis. Following Jiang et al. (2012), considering the eastward propagating MJO signals are mainly confined near the equator over the Indo-Pacific, the anomalies are averaged between 10°S and 15°N for the longitudes from 60°E to 150°W; whereas for the eastern Pacific domain from 150° to 80°W, the anomalies are averaged between 5° and 15°N, since the EPAC ISV has an off-equatorial domain of activity. It is clearly evident that when the MJO signal is weak, the EPAC ISV amplitude is weak in both fields. Moreover, a strong physical link between eastern and western Pacific ISV is readily discerned in both precipitation and wind anomalies when the western Pacific MJO is active (Fig. 8a) but is not evident when the MJO is weak (Fig. 8b). In the latter case, the systematic eastward propagation is only observed to the east of 120°W and appears more local in origin. The results are similar when quiescent MJO condition is defined using a threshold of RMM amplitude <0.8. Thus it suggests that even in the absence of propagating MJO signals from the west, the EPAC ISV might still exist by itself, although at a weaker amplitude. While the possibility of remote forcing from western Pacific cannot be ruled out, even in the absence of an organized large-scale MJO propagating signal, it can be assumed that local convection circulation feedbacks might have an

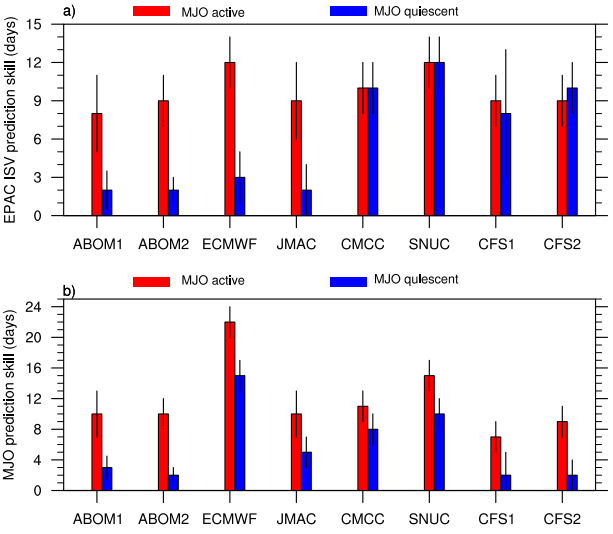

FIG. 9. (a) Average individual hindcast prediction skill for PC1 in the eight models for hindcasts initiated from active MJO conditions (RMM amplitude >1.2; red bars) and quiescent MJO conditions (RMM amplitude <0.8; blue bars). (b) The MJO prediction skill in the eight models for the same set of cases considered in (a). In each panel, the error bars represent the 95% confidence estimates for the correlation-based prediction skill.

upper hand in sustaining the EPAC ISV when the MJO forcing is weak. Wang and Zhang (2002) showed how atmosphere–ocean interaction in the presence of a background convergence zone was responsible for the maintenance of the ISV over the western and northern Pacific. A similar mechanism might be at work over the EPAC ISV domain. In the next section we further explore whether the presence or absence of MJO forcing has any direct implications on the EPAC ISV prediction in the ISVHE models.

The hindcasts are grouped based on the MJO being active (RMM amplitude >1.2) or quiescent (RMM amplitude <0.8) on the day of hindcast initiation, and the average individual hindcast prediction skill for these two cases was shown in Fig. 9a. For a comparison, the corresponding MJO prediction skill estimates in these eight models are also shown in Fig. 9b. Note that the MJO prediction skill shown here is based on the bivariate correlation (H. Lin et al. 2008; Rashid et al. 2011) using the RMM1 and RMM2 indices computed from each model hindcast following Neena et al. (2014). From Figs. 9a and 9b it is evident that, when the hindcasts are initiated from active MJO conditions, the relative skill of a model for the EPAC ISV is related to its skill in predicting the MJO (the correlation between the red bars in Figs. 9a and 9b is 0.85). In four models—ABOM1, ABOM2, ECMWF, and JMAC—the MJO prediction skill and the EPAC ISV hindcast skill are significantly lower in hindcasts initiated from weak or quiescent MJO conditions (Figs. 9a,b, blue bars) as compared to those from hindcasts initiated during active MJO conditions. In the other four models (CMCC, SNUC, CFS1, and CFS2), even though the MJO prediction skill associated with quiescent MJO initial conditions is lower than that associated with active MJO conditions, the EPAC ISV prediction skill seems largely unaffected by the presence or absence of MJO during hindcast initiation. One possibility is that in the former four models the EPAC ISV is mainly forced by the global MJO signal and in the latter four models the EPAC ISV mode is more locally driven. Another possibility could be that the local generation mechanisms for the EPAC ISV are poorly represented in the former set of models or the teleconnection mechanisms across the Pacific are poorly represented in the latter set of models, or both.

This above hypothesis is further tested by performing a simple analysis of the relationship between the EPAC ISV and the western Pacific precipitation variability in the model hindcasts. For each model, for each lead day of hindcast, correlations between the $PC1_{hcast}$ and hindcast precipitation anomalies were computed at every grid point in the equatorial domain (15°S–25°N, 120°E–80°W). If, as suspect, in the latter set of models (CMCC, SNUC, CFS1, and CFS2) the EPAC-ISV evolution is less dependent on the west Pacific MJO, the correlation fields should give some indication of this by being lower in these models. The spatial distribution of the multimodel average correlation coefficient values for the hindcasts from the two sets of models are shown in Figs. 10a and 10b. The spatial distribution of correlation coefficients based on the hindcasts from ABOM1, ABOM2, ECMWF, and JMAC models, at 1-, 3-, 6-, and 9-day hindcast leads are shown in Fig. 10a, and similarly for the CMCC, SNUC, CFS1, and CFS2 models in Fig. 10b. In Fig. 10a, a band of negative correlation values can be seen extending from the western to the central Pacific. The slightly weaker negative correlation values over the western and central Pacific in Fig. 10b gives some indication of a weaker relationship between the eastern and western Pacific in the hindcasts from the latter four models (Fig. 10b). The differences are evident even at 9-day lead. While noteworthy, it is not possible to make any comprehensive conclusions on the nature of the EPAC ISV–MJO relationship in the models, based on the correlation fields of daily hindcast anomalies. Nevertheless, the analysis signals the need to carry out detailed investigations of the MJO–EPAC ISV relationship in GCMs and it also indicates the importance of such understanding for improving EPAC ISV predictions.

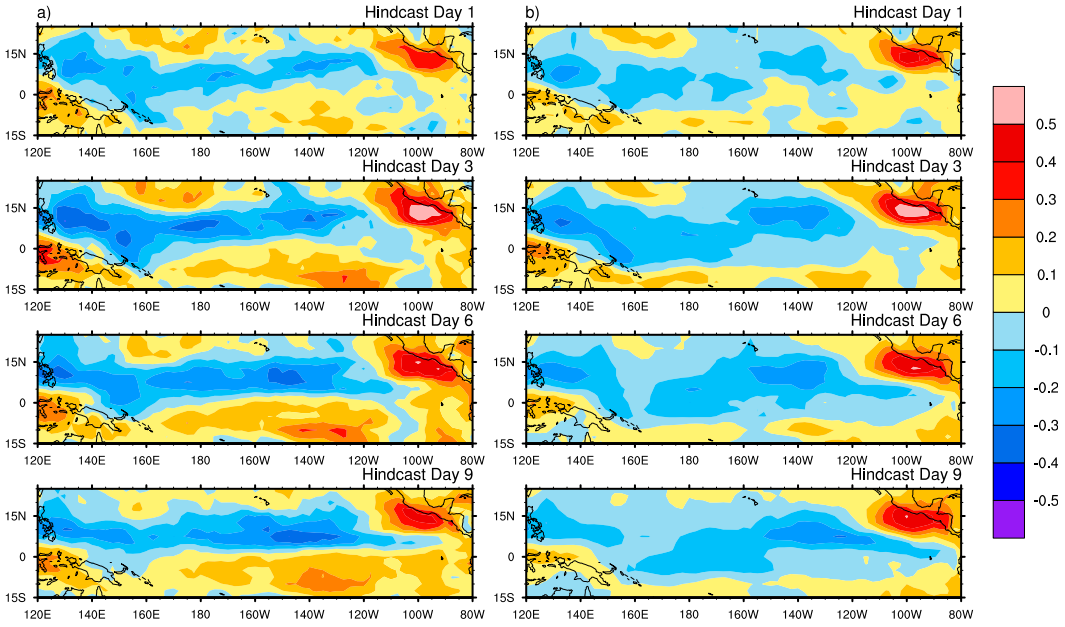

FIG. 10. Spatial distribution of correlation coefficients between $PC1_{hcast}$ and hindcast precipitation anomalies over the equatorial domain (15°S–25°N, 120°E–80°W), at 1-, 3-, 6-, and 9-day hindcast leads: (a) multimodel average correlations based on the ABOM1, ABOM2, ECMWF, and JMAC model hindcasts and (b) multimodel average correlations based on the CMCC, SNUC, CFS1, and CFS2 model hindcasts.

7. Conclusions

For the first time, the dynamical prediction skill and predictability for the dominant summer ISV mode over the eastern Pacific are explored by analyzing hindcast data from eight coupled models that participated in the ISVHE. The leading ISV mode over the EPAC was isolated through a multivariate EOF analysis of precipitation and U850. The results indicate a smaller lead time of dynamical prediction skill for the EPAC ISV than for the boreal winter MJO (15–25 days), with prediction skill ranging from 10 to 14 days in the eight models analyzed. The predictability for the leading EPAC ISV mode was further explored using perfect model assumption and it was estimated to be in the 20–30-day range. Previous analysis of EPAC ISV simulations in dynamic models and the results from this study indicate that faithful simulations and prediction of the EPAC ISV still remain a great challenge for present-day GCMs. The convective to subsidence transition phase seems to have a higher predictability than the subsidence to convective phase transition over the EPAC domain, implied by the higher prediction skill associated with hindcasts initiated from convective phase of EPAC ISV and considerations of the relevant forecast lead times and ISV time scale. The EPAC ISV–MJO relationship was also explored using the leading EPAC ISV modes and the RMM indices. It was noted that a major fraction (68%) of EPAC ISV convective events occurred in conjunction with active MJO conditions and the seesaw structure of convection was apparent over the eastern and western Pacific domains. The EPAC ISV during quiescent MJO conditions was found to be weak and more localized. The prediction skill of the EPAC ISV associated with these contrasting MJO conditions was explored in the eight model hindcasts. In four of the eight models, higher EPAC ISV prediction skill was associated with hindcasts initiated during active MJO conditions as compared to the skill in hindcasts initiated from quiescent MJO conditions. In the other models the skill associated with hindcasts initiated from quiescent MJO conditions was as high as that associated with active conditions. We speculate that, in the models that exhibit EPAC ISV prediction skill sensitivity to MJO strength, at least in the hindcast mode, the EPAC ISV might be mainly forced by the global MJO signal or the mechanisms for local generation of the EPAC ISV might not be in place. And, for the other four models, local convection–circulation feedback might have an upper hand over MJO forcing in maintaining the EPAC ISV, or the teleconnection mechanisms for east–west Pacific communications might not be adequately represented. Again, there is the possibility of other remote forcing mechanisms that are not yet explored. Similar to the results for EPAC ISV simulation in different dynamic models (Jiang et al. 2012), the behavior of model

hindcasts in this study also point to the fact that the representation of EPAC ISV–MJO relationship might be significantly different in different dynamical models. Understanding this dynamic link and quantifying the relative roles of MJO forcing and local effects in the maintenance of EPAC ISV would be crucial for the simulation and prediction of this mode. The EPAC ISV is also known to exhibit a 16-day lag (or out of phase) relationship with the boreal summer ISV mode over northern Indian Ocean (Wang et al. 2006; Moon et al. 2013), which would again be an interesting aspect to explore in EPAC ISV research. The limited prediction skill for the EPAC ISV in dynamic models, a promising 20–30 days of predictability, and the underexplored relationship with the MJO and other large-scale modes call for focused efforts in simulating and predicting the EPAC ISV mode in dynamic models.

Acknowledgments. The authors thank all the participating members of ISVHE project for the dataset. This work was supported by NOAA's Climate Program Office CTB Program under Grant GC10287a and MAPP Program under Grant NA12OAR4310075, the Office of Naval Research under Project ONRBAA12-001, and NSF Climate and Large-Scale Dynamics Program under Awards AGS-1221013 and AGS-1228302. Part of this research was carried out at the Jet Propulsion Laboratory, California Institute of Technology, under a contract with the National Aeronautics and Space Administration.

REFERENCES

Dee, D. P., and Coauthors, 2011: The ERA-Interim reanalysis: Configuration and performance of the data assimilation system. *Quart. J. Roy. Meteor. Soc.,* **137,** 553–597, doi:10.1002/qj.828.

Fisher, R. A., 1921: On the ''probable error'' of a coefficient of correlation deduced from a small sample. *Metron,* **1,** 3–32.

Fu, X., B. Wang, D. E. Waliser, and L. Tao, 2007: Impact of atmosphere–ocean coupling on the predictability of monsoon intraseasonal oscillations. *J. Atmos. Sci.,* **64,** 157–174, doi:10.1175/JAS3830.1.

Higgins, R. W., and W. Shi, 2001: Intercomparison of the principal modes of interannual and intraseasonal variability of the North American monsoon system. *J. Climate,* **14,** 403–417, doi:10.1175/1520-0442(2001)014<0403:IOTPMO>2.0.CO;2.

Huffman, G. J., and Coauthors, 2007: The TRMM Multisatellite Precipitation Analysis (TMPA): Quasi-global, multiyear, combined-sensor precipitation estimates at fine scales. *J. Hydrometeor.,* **8,** 38–55, doi:10.1175/JHM560.1.

Jiang, X., and D. E. Waliser, 2008: Northward propagation of the subseasonal variability over the eastern Pacific warm pool. *Geophys. Res. Lett.,* **35,** L09814, doi:10.1029/2008GL033723.

——, and ——, 2009: Two dominant subseasonal variability modes of the eastern Pacific ITCZ. *Geophys. Res. Lett.,* **36,** L04704, doi:10.1029/2008GL036820.

——, M. Zhao, and D. E. Waliser, 2012: Modulation of tropical cyclones over the eastern Pacific by the intraseasonal variability simulated in an AGCM. *J. Climate,* **25,** 6524–6538, doi:10.1175/JCLI-D-11-00531.1.

——, E. D. Maloney, J.-L. F. Li, and D. E. Waliser, 2013: Simulations of the eastern North Pacific intraseasonal variability in CMIP5 GCMs. *J. Climate,* **26,** 3489–3510, doi:10.1175/JCLI-D-12-00526.1.

Kayano, M., and V. Kousky, 1999: Intraseasonal (30–60 day) variability in the global tropics: Principal modes and their evolution. *Tellus,* **51,** 373–386, doi:10.1034/j.1600-0870.1999.t01-3-00003.x.

Kikuchi, K., and B. Wang, 2009: Global perspectives of the quasi-biweekly oscillation. *J. Climate,* **22,** 1340–1359, doi:10.1175/2008JCLI2368.1.

Kiladis, G. N., J. Dias, K. H. Straub, M. C. Wheeler, S. N. Tulich, K. Kikuchi, K. M. Weickmann, and M. J. Ventrice, 2014: A comparison of OLR and circulation based indices for tracking the MJO. *Mon. Wea. Rev.,* **142,** 1697–1715, doi:10.1175/MWR-D-13-00301.1.

Knutson, T. R., and K. M. Weickmann, 1987: 30–60 day atmospheric circulations: Composite life cycles of convection and circulation anomalies. *Mon. Wea. Rev.,* **115,** 1407–1436, doi:10.1175/1520-0493(1987)115<1407:DAOCLC>2.0.CO;2.

Lau, W. K.-M., and D. E. Waliser, Eds., 2012: *Intraseasonal Variability in the Atmosphere–Ocean Climate System.* 2nd ed. Springer, 613 pp.

Lee, J.-Y., B. Wang, M. C. Wheeler, X. Fu, D. E. Waliser, and I.-S. Kang, 2013: Real-time multivariate indices for the boreal summer intraseasonal oscillation over the Asian summer monsoon region. *Climate Dyn.,* **40,** 493–509, doi:10.1007/s00382-012-1544-4.

Liess, S., D. E. Waliser, and S. Schubert, 2005: Predictability studies of the intraseasonal oscillation with the ECHAM5 GCM. *J. Atmos. Sci.,* **62,** 3320–3336, doi:10.1175/JAS3542.1.

Lin, H., G. Brunet, and J. Derome, 2008: Forecast skill of the Madden–Julian oscillation in two Canadian atmospheric models. *Mon. Wea. Rev.,* **136,** 4130–4149, doi:10.1175/2008MWR2459.1.

Lin, J.-L., B. E. Mapes, K. M. Weickmann, G. N. Kiladis, S. D. Schubert, M. J. Suarez, J. T. Bacmeister, and M.-I. Lee, 2008: North American monsoon and convectively coupled equatorial waves simulated by IPCC AR4 coupled GCMs. *J. Climate,* **21,** 2919–2937, doi:10.1175/2007JCLI1815.1.

Lorenz, D. J., and D. L. Hartmann, 2006: The effect of the MJO on the North American monsoon. *J. Climate,* **19,** 333–343, doi:10.1175/JCLI3684.1.

Magaña, V., J. A. Amador, and S. Medina, 1999: The midsummer drought over Mexico and Central America. *J. Climate,* **12,** 1577–1588, doi:10.1175/1520-0442(1999)012<1577:TMDOMA>2.0.CO;2.

Maloney, E. D., and D. L. Hartmann, 2000a: Modulation of eastern North Pacific hurricanes by the Madden–Julian oscillation. *J. Climate,* **13,** 1451–1460, doi:10.1175/1520-0442(2000)013<1451:MOENPH>2.0.CO;2.

——, and ——, 2000b: Modulation of hurricane activity in the Gulf of Mexico by the Madden–Julian oscillation. *Science,* **287,** 2002–2004, doi:10.1126/science.287.5460.2002.

——, and J. T. Kiehl, 2002: Intraseasonal eastern Pacific precipitation and SST variations in a GCM coupled to a slab ocean model. *J. Climate,* **15,** 2989–3007, doi:10.1175/1520-0442(2002)015<2989:IEPPAS>2.0.CO;2.

——, and S. K. Esbensen, 2005: A modeling study of summertime east Pacific wind-induced ocean–atmosphere exchange in the intraseasonal oscillation. *J. Climate,* **18,** 568–584, doi:10.1175/JCLI-3280.1.

——, and ——, 2007: Satellite and buoy observations of boreal summer intraseasonal variability in the tropical northeast Pacific. *Mon. Wea. Rev.,* **135,** 3–19, doi:10.1175/MWR3271.1.

——, D. B. Chelton, and S. K. Esbensen, 2008: Subseasonal SST variability in the tropical eastern North Pacific during boreal summer. *J. Climate,* **21,** 4149–4167, doi:10.1175/2007JCLI1856.1.

——, X. Jiang, S.-P. Xie, and J. J. Benedict, 2014: Process-oriented diagnosis of east Pacific warm pool intraseasonal variability. *J. Climate,* **27,** 6305–6324, doi:10.1175/JCLI-D-14-00053.1.

Martin, E. R., and C. Schumacher, 2011: Modulation of Caribbean precipitation by the Madden–Julian oscillation. *J. Climate,* **24,** 813–824, doi:10.1175/2010JCLI3773.1.

Moon, J. Y., B. Wang, K.-J. Ha, and J.-Y. Lee, 2013: Teleconnections associated with Northern Hemisphere summer monsoon intraseasonal oscillation. *Climate Dyn.,* **40,** 2761–2774, doi:10.1007/s00382-012-1394-0.

Neena, J. M., and B. N. Goswami, 2010: Extension of potential predictability of Indian summer monsoon dry and wet spells in recent decades. *Quart. J. Roy. Meteor. Soc.,* **136,** 583–592, doi:10.1002/qj.595.

——, J. Y. Lee, D. E. Waliser, B. Wang and X. Jiang, 2014: Predictability of the Madden Julian oscillation in the Intraseasonal Variability Hindcast Experiment (ISVHE). *J Climate,* **27,** 4531–4543, doi:10.1175/JCLI-D-13-00624.1.

Pegion, K., and B. Kirtman, 2008: The impact of air–sea interactions on the predictability of the tropical intraseasonal oscillation. *J. Climate,* **21,** 5870–5886, doi:10.1175/2008JCLI2209.1.

Rashid, H. A., H. H. Hendon, M. C. Wheeler, and O. Alves, 2011: Prediction of the Madden–Julian oscillation with the POAMA dynamical prediction system. *Climate Dyn.,* **36,** 649–661, doi:10.1007/s00382-010-0754-x.

Rydbeck, A. V., E. D. Maloney, S.-P. Xie, J. Hafner, and J. Shaman, 2013: Remote forcing versus local feedback of east Pacific intraseasonal variability during boreal summer. *J. Climate,* **26,** 3575–3596, doi:10.1175/JCLI-D-12-00499.1.

Seo, K.-H., W. Wang, J. Gottschalck, Q. Zhang, J.-K. E. Schemm, W. R. Higgins, and A. Kumar, 2009: Evaluation of MJO forecast skill from several statistical and dynamical forecast models. *J. Climate,* **22,** 2372–2388, doi:10.1175/2008JCLI2421.1.

Serra, Y. L., G. N. Kiladis, and K. I. Hodges, 2010: Tracking and mean structure of easterly waves over the Intra-Americas Sea. *J. Climate,* **23,** 4823–4840, doi:10.1175/2010JCLI3223.1.

Small, R. J., S. P. de Szoeke, and S.-P. Xie, 2007: The Central American midsummer drought: Regional aspects and large-scale forcing. *J. Climate,* **20,** 4853–4873, doi:10.1175/JCLI4261.1.

——, S.-P. Xie, E. D. Maloney, S. P. deSzoeke, and T. Miyama, 2011: Intraseasonal variability in the far-east Pacific: Investigation of the role of air–sea coupling in a regional coupled model. *Climate Dyn.,* **36,** 867–890, doi:10.1007/s00382-010-0786-2.

Vitart, F., and F. Molteni, 2010: Simulation of the Madden–Julian oscillation and its teleconnections in the ECMWF forecast system. *Quart. J. Roy. Meteor. Soc.,* **136,** 842–855, doi:10.1002/qj.623.

——, S. Woolnough, M. A. Balmaseda, and A. M. Tompkins, 2007: Monthly forecast of the Madden–Julian oscillation using a coupled GCM. *Mon. Wea. Rev.,* **135,** 2700–2715, doi:10.1175/MWR3415.1.

Waliser, D. E., 2011: Predictability and forecasting. *Intraseasonal Variability of the Atmosphere–Ocean Climate System,* 2nd ed. W. K. M. Lau and D. E. Waliser, Eds., Springer, 433–476.

——, K. M. Lau, W. Stern, and C. Jones, 2003a: Potential predictability of the Madden–Julian oscillation. *Bull. Amer. Meteor. Soc.,* **84,** 33–50, doi:10.1175/BAMS-84-1-33.

——, W. Stern, S. Schubert, and K. M. Lau, 2003b: Dynamic predictability of intraseasonal variability associated with the Asian summer monsoon. *Quart. J. Roy. Meteor. Soc.,* **129,** 2897–2925, doi:10.1256/qj.02.51.

Wang, B., 1992: The vertical structure and development of the ENSO anomaly mode during 1979–1989. *J. Atmos. Sci.,* **49,** 698–712, doi:10.1175/1520-0469(1992)049<0698:TVSADO>2.0.CO;2.

——, and Q. Zhang, 2002: Pacific–East Asian teleconnection. Part II: How the Philippine Sea anticyclone is established during development of El Nino. *J. Climate,* **15,** 3252–3265, doi:10.1175/1520-0442(2002)015<3252:PEATPI>2.0.CO;2.

——, P. Webster, K. Kikuchi, T. Yasunari, and Y. Qi, 2006: Boreal summer quasi-monthly oscillation in the global tropics. *Climate Dyn.,* **27,** 661–675, doi:10.1007/s00382-006-0163-3.

Wang, W., M.-P. Hung, S. J. Weaver, A. Kumar, and X. Fu, 2014: MJO prediction in the NCEP Climate Forecast System version 2. *Climate Dyn.,* **42,** 2509–2520, doi:10.1007/s00382-013-1806-9.

Wen, M., S. Yang, W. Higgins, and R. Zhang, 2011: Characteristics of the dominant modes of atmospheric quasi-biweekly oscillation over tropical–subtropical Americas. *J. Climate,* **24,** 3956–3970, doi:10.1175/2011JCLI3916.1.

Wheeler, M. C., and H. H. Hendon, 2004: An all-season real-time multivariate MJO index: Development of an index for monitoring and prediction. *Mon. Wea. Rev.,* **132,** 1917–1932, doi:10.1175/1520-0493(2004)132<1917:AARMMI>2.0.CO;2.

Zhang, C., 2005: The Madden–Julian oscillation. *Rev. Geophys.,* **43,** RG2003, doi:10.1029/2004RG000158.

Zhang, Q., and H. Van den Dool, 2012: Relative merit of model improvement versus availability of retrospective forecasts: The case of climate forecast system MJO prediction. *Wea. Forecasting,* **27,** 1045–1051, doi:10.1175/WAF-D-11-00133.1.